Carrier-driven bipolar magnetic semiconductor behavior and half-metallicity with large anomalous Hall effect in antiferromagnetic monolayer $CuPdBr_3$

Jiexue Li,[1] Xuan Wang,[1] Jiahui Qian,[2,3] Xunkai Duan,[2,3] Chunlan Ma,[1] Tong Zhou,[2,*] and Jiayong Zhang[1,2,†]

[1]*Key Laboratory of Efficient Low-Carbon Energy Conversion and Utilization of Jiangsu Provincial Higher Education Institutions, School of Physical Science and Technology, Suzhou University of Science and Technology, Suzhou 215009, China*

[2]*Eastern Institute for Advanced Study, Eastern Institute of Technology, Ningbo, Zhejiang 315200, China*

[3]*School of Physics and Astronomy, Shanghai Jiao Tong University, Shanghai 200240, China*

(Received 20 December 2025; accepted 16 September 2026; published 5 October 2026)

Two-dimensional magnetic materials with tunable electronic and magnetic properties show great potential for spintronic applications. Using first-principles calculations, we systematically investigate monolayer $CuPdBr_3$ and identify it as a zigzag antiferromagnetic (AF-Zigzag) semiconductor with an indirect band gap. While the AF-Zigzag ground state remains robust under strain, its magnetic configuration can be effectively tuned through carrier doping. Notably, both electron and hole doping induce a magnetic phase transition from the AF-Zigzag to a ferromagnetic (FM) state, with the stability of the FM state enhanced by increasing doping concentration. The corresponding critical temperature can be increased to about 100 K. Remarkably, antiferromagnetic (AFM) monolayer $CuPdBr_3$, driven by carrier doping, behaves as a bipolar magnetic semiconductor (BMS). In the FM state induced by hole doping, the spin-up channel becomes metallic, giving rise to a ferromagnetic half-metal (FMHM), whereas electron doping results in a FMHM with a metallic spin-down channel. The carrier-doping-induced BMS behavior of AFM monolayer $CuPdBr_3$ suggests its potential application in spin field-effect transistor devices. Furthermore, in carrier-doped monolayer $CuPdBr_3$ with the FM state, spin-orbit coupling opens energy gaps around the spin-polarized non-Dirac band degeneracies at the Γ point, resulting in significant anomalous Hall conductivity. These findings highlight AFM monolayer $CuPdBr_3$ as a promising candidate for the development of two-dimensional antiferromagnet-based spintronic devices and the exploration of novel magnetic phenomena.

DOI: 10.1103/f1dy-6nwp

I. INTRODUCTION

Two-dimensional (2D) materials have captured substantial interest in condensed matter physics and materials science, driven by their potential for enabling high-performance electronic and spintronic devices. Since the discovery of graphene [1], the exploration of 2D materials has expanded to encompass a wide range of novel systems, including silicene [2], h-BN [3], black phosphorus [4], bismuthine [5], and transition metal (TM) dichalcogenides MX_2 (TMDs) [6,7]. Despite the growing variety of 2D materials, most have been found to be nonmagnetic. However, the recent emergence of 2D magnetic materials, characterized by their unique physical properties and potential applications in magnetism and spintronics [8,9], has generated considerable interest in the 2D materials research field. For magnetic metals, half-metals [10], have emerged as key materials for spintronics. These materials feature a metallic single-spin channel, while the opposite spin channel remains insulating or semiconducting, thereby enabling single-spin-channel transport. Bipolar magnetic semiconductors (BMSs) [11] and half magnetic semiconductors (HMSs) [8] are two types of ideal spintronic materials for magnetic semiconductors. BMSs exhibit unique band structures in which the conduction band minimum (CBM) and valence band maximum (VBM) belong to opposite spin channels [11]. In contrast, HMSs feature both the VBM and CBM belonging to the same spin channel [8]. BMSs allow control of the spin orientation of the conducting carriers by reversing the polarity of the applied gate voltage [8,11], enabling the Fermi energy (E_F) to be tuned into half-metallic states with either a spin-up or a spin-down single-spin conducting channel. In comparison, HMSs enable the generation of both electron and hole carriers through the same single-spin conducting channel under positive and negative gate voltages [8], respectively. Given these promising properties, half-metals, BMSs, and HMSs have great potential for advancing spintronic devices, making them important materials for future spintronics research.

Up to now, several types of 2D magnetic materials have been theoretically predicted via first-principles calculations. Among these, monolayer TM trichalcogenides ABX_3 [12–14], monolayer TM trihalides MX_3 [15–20], functionalized honeycomb atomic monolayers [21–26], layered TM thio(seleno)phosphates [27–29], and layered MA_2Z_4-family materials [30–32] are significant 2D magnetic materials that have been extensively studied. These materials are predicted to exhibit lots of novel physical properties, such as 2D intrinsic ferromagnetic (FM) semiconductors in CrI_3 [15] and

*Contact author: tzhou@eitech.edu.cn
†Contact author: jyzhang@usts.edu.cn

 ©2026 American Physical Society

$CrGeTe_3$ [12], antiferroelectric altermagnets in $CuWP_2S_6$ [33], ferroelectric altermagnets in monolayer VOI_2 [34], and tunable magnetic topologically nontrivial states in layered $MnBi_2Te_4$ [31,32]. Experimental advancements have led to significant progress. Notably, monolayer CrI_3 [35] and bilayer $CrGeTe_3$ [36] have been successfully synthesized and confirmed as intrinsic 2D FM semiconductors. Additionally, the quantum anomalous Hall (QAH) effect has been experimentally realized in layered $MnBi_2Te_4$ [37], further validating theoretical predictions. These discoveries have paved the way for more detailed investigations into 2D magnetic materials. The tunability of magnetic properties through external means, such as strain and carrier doping [13,38–41], has emerged as a powerful approach. Sivadas *et al.* [13] demonstrated that strain could effectively modulate the magnetic properties of monolayer $AB X_3$. Li *et al.* [38] predicted that both electron and hole doping could induce the magnetic phase transition in monolayer $MnPSe_3$ from an antiferromagnetic (AFM) state to a FM state. Wang *et al.* [39] predicted that hole doping could tune monolayer CrI_3 to exhibit room-temperature FM half-metallicity. Zhang *et al.* [40] proposed that strain and carrier doping could be employed to adjust the magnetic ground state and spintronics behaviors of monolayer MoX_3 (X = Cl, Br, I). These findings collectively highlight that strain and carrier doping are effective methods for manipulating the magnetic structures and spintronic properties of 2D magnetic materials. Such tunability not only deepens the understanding of 2D magnetism but also opens avenues for designing novel electronic and spintronic devices.

In this work, we systematically investigate the tunability of electronic structures, magnetic properties, and spintronic behaviors in monolayer $CuPdBr_3$ through strain engineering and carrier doping, using first-principles calculations. Our results reveal that monolayer $CuPdBr_3$ is in the zigzag antiferromagnetic (AF-Zigzag) state and is an indirect band gap semiconductor. The AF-Zigzag ground state is robust against strain, whereas the magnetic configuration of monolayer $CuPdBr_3$ can be effectively tuned via carrier doping. The magnetic phase diagrams reveal that the FM state can be achieved through either electron or hole doping, with the critical temperature (T_C) increasing linearly with carrier doping concentration. Remarkably, AFM monolayer $CuPdBr_3$, driven by carrier doping, behaves as a BMS. Specifically, hole doping induces a FM half-metal (FMHM) state with a spin-up conducting channel, whereas electron doping leads to a FMHM state with a spin-down conducting channel. Furthermore, the carrier-doping-induced BMS behavior of AFM monolayer $CuPdBr_3$ suggests its potential application in spin field-effect transistor (Spin-FET) devices. Additionally, in carrier-doped monolayer $CuPdBr_3$ in the FM state, spin-orbit coupling (SOC) opens energy gaps around the spin-polarized non-Dirac band degeneracies at the Γ point, leading to large anomalous Hall conductivity.

II. COMPUTATIONAL DETAILS

The first-principles calculations are performed by using the projected augmented-wave (PAW) [42] formalism based on density functional theory (DFT), as implemented in the Vienna *Ab initio* Simulation Package (VASP) [43]. The Perdew-Burke-Ernzerhof generalized gradient approximation (GGA-PBE) is employed to describe the exchange and correlation functional [44]. The GGA + U [45] is adopted to account for the correlation effects of the Pd 4d electrons, with the on-site Coulomb interaction U and exchange interaction J set to 3.0 and 1.0 eV, respectively. To examine the robustness of the magnetic ground state with respect to the Hubbard U parameters, additional benchmark calculations were performed by varying the effective Hubbard U values on both Cu and Pd atoms. Furthermore, HSE06 calculations were carried out for both the pristine monolayer and representative electron- and hole-doped cases. Details of these benchmark calculations are provided in the Supplemental Material [46]. The plane-wave energy cutoff and the total energy convergence criterion are set to 550 and 10^{-6} eV, respectively. A vacuum space of 20 Å is introduced to prevent interactions between adjacent slabs. All atoms in the unit cell are allowed to relax until the Hellmann-Feynman force on each atom is smaller than 0.01 eV/Å. The $11 \times 11 \times 1$ and $11 \times 6 \times 1$ Gamma central Monkhorst-Pack grids are adopted during the calculations for the unit cell (with $Cu_2Pd_2Br_6$) and rectangular supercell (with $Cu_4Pd_4Br_{12}$), respectively. The GGA-PBE method is adopted to calculate the lattice constant of monolayer $CuPdBr_3$. To examine the dynamical stability, The phonon spectrum is calculated by using the PHONOPY code [47] combined with VASP. *Ab initio* molecular dynamics (AIMD) simulations are carried out to investigate the thermal stability. The Monte Carlo (MC) simulations based on the classical 2D Heisenberg model are performed to estimate the T_C. The maximally localized Wannier functions (MLWFs) [48,49] are constructed by using the WANNIER90 package [50], and the Berry curvatures and anomalous Hall conductivity are calculated by employing the algorithm described in Ref. [51].

III. RESULTS AND DISCUSSION

A. Crystal structure and stabilities

The atomic structure of monolayer $CuPdBr_3$, shown in Figs. 1(a) and 1(b), consists of three atomic layers, with the Pb atomic layer positioned in the center, sandwiched between two Br-Cu atomic layers. The unit cell of monolayer $CuPdBr_3$ contains two Cu atoms, two Pd atoms, and six Br atoms. The Pd atoms form a 2D honeycomb lattice, and each Pd atom is surrounded by six nearest-neighbor (NN) Br atoms, forming an edge-sharing distorted octahedron, as shown in Fig. 1(b2). In addition, the Cu atoms within each Br-Cu layers form a 2D triangular lattice. The atomic structure of monolayer $CuPdBr_3$ is derived from monolayer $PdBr_3$ by decorating two Cu atoms at the hexagonal hollow sites formed by the top and bottom Br atomic layers in the unit cell, resembling the crystal structure of monolayer TM trichalcogenides ABX_3 [12–14]. The optimized equilibrium lattice constant of monolayer $CuPdBr_3$ is $a = 6.78$ Å. In monolayer $CuPdBr_3$, the vertical distance between two Br atomic planes is 3.09 Å, the NN Pd-Pd distance is 3.92 Å, and the Pd-Br-Pd bond angle is 93.15°.

The structural stabilities of the monolayer $CuPdBr_3$ are examined by the formation energy calculations, phonon spectrum calculations, and AIMD simulations. The formation energy of monolayer $CuPdBr_3$ is defined as

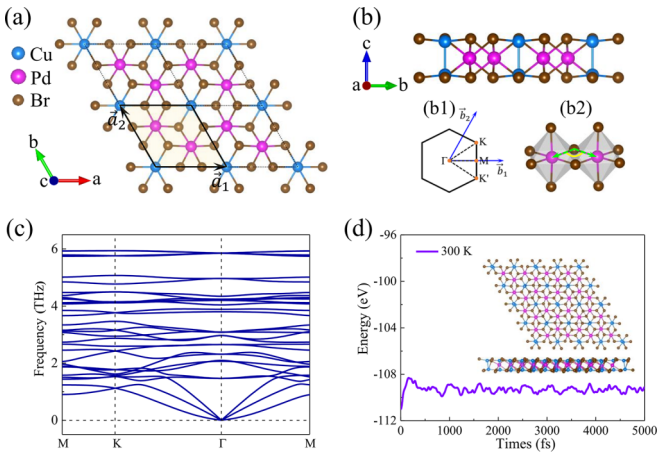


FIG. 1. (a), (b) Top and side views of the atomic structure of monolayer $CuPdBr_3$. The rhombus in (a) shows the unit cell with lattice vectors $\vec{a}_1$ and $\vec{a}_2$. The bottom insets in (b) show: (b1) First Brillouin zone with high symmetry points; (b2) Bromine octahedron. (c) Phonon spectrum for monolayer $CuPdBr_3$. (d) AIMD simulations at 300 K. The insets in (d) display atomic configuration snapshots from AIMD simulations after 5.0 ps.

$E_{\text{form}} = E(\text{CuPdBr}_3) - 2E(\text{Cu}) - 2E(\text{Pd}) - 3E(\text{Br}_2)$, where $E(\text{CuPdBr}_3)$ is the total energy of the monolayer $CuPdBr_3$ unit cell, $E(\text{Cu})$ is the total energy of the bulk Cu in the face-centered-cubic unit cell with one Cu atom, $E(\text{Pd})$ is the total energy of bulk Pd in the face-centered-cubic unit cell with one Pd atom, and $E(\text{Br}_2)$ is the total energy of the Br_2 molecule. The calculated formation energy is $E_{\text{form}} = -3.66\,\text{eV}$, indicating that monolayer $CuPdBr_3$ will form a strongly bonded network. The calculated phonon spectrum is shown in Fig. 1(c), from which we can find that there is no imaginary-frequency mode in the whole Brillouin zone (BZ), indicating the dynamical stability of the monolayer $CuPdBr_3$. The fluctuation of total energies of the monolayer $CuPdBr_3$ system with respect to time during AIMD simulations at 300 K is plotted in Fig. 1(d). The insets in Fig. 1(d) show the top and side views of atomic configuration snapshots from the AIMD simulations after 5.0 ps at 300 K, from which we can find that monolayer $CuPdBr_3$ can maintain its structural integrity, indicating the thermal stability of the monolayer $CuPdBr_3$. According to the calculated formation energy, phonon spectrum, and AIMD simulations, the crystal structure of monolayer $CuPdBr_3$ is both dynamically and thermally stable at room temperature.

To further evaluate the potential experimental feasibility of obtaining monolayer $CuPdBr_3$, we constructed a hypothetical layered bulk $CuPdBr_3$ model based on the common structural motif of layered transition-metal halides and calculated its cleavage energy. As shown in Fig. S4 of the Supplemental Material [46], the calculated cleavage energy converges to approximately 0.31 J/m^2, which is comparable to those of experimentally exfoliated layered materials such as graphene ($\sim$0.37 J/m^2) and MoS_2 ($\sim$0.27–0.35 J/m^2). The relatively small cleavage energy indicates weak interlayer binding and suggests that mechanical exfoliation of monolayer $CuPdBr_3$ would be feasible if such a layered bulk phase can be experimentally realized in the future.

B. Magnetic properties and carrier-doping-induced FM state

The magnetization in monolayer $CuPdBr_3$ is primarily contributed by the Pd atoms. Each Pd atom exhibits a local magnetic moment of approximately 2.0 μ_B. To determine the magnetic ground state, we examine four representative magnetic configurations: FM, AF-Néel, AF-Zigzag, and AF-Stripy, as shown in Figs. 2(a1)–2(a4). The total energies of the four different magnetic configurations are calculated by using a rectangular supercell ($Cu_4Pd_4Br_{12}$), as shown in Fig. 2(a). The energy differences (ΔE) for $E_{\text{AF-Néel}} - E_{\text{FM}}$, $E_{\text{AF-Zigzag}} - E_{\text{FM}}$, and $E_{\text{AF-Stripy}} - E_{\text{FM}}$ are 50.3 meV, -23.0 meV, and 31.8 meV, respectively, indicating that the AF-Zigzag configuration is the magnetic ground state of monolayer $CuPdBr_3$, as shown in Fig. 2(b).

To further examine the reliability of the magnetic ground state, we systematically investigated the dependence of magnetic ordering on the Hubbard U parameters. The calculated magnetic energy differences show that varying the effective Hubbard U_{eff} correction on Cu from 0.0 to 5.0 eV has negligible influence on the relative stability of different magnetic configurations. Moreover, the AF-Zigzag state remains the lowest-energy configuration throughout the investigated Pd-U_{eff} range from 0.0 to 4.0 eV, demonstrating the robustness of the magnetic ground state of monolayer $CuPdBr_3$ within the PBE + U framework (see Figs. S1 and S2 in the Supplemental Material [46]). Considering that the magnetic moment of monolayer $CuPdBr_3$ mainly originates from the Pd 4d orbitals, a Hubbard correction was applied to Pd 4d states. The adopted $U_{\text{eff}} = U - J = 2.0\,\text{eV}$ value for Pd 4d orbitals was chosen based on previous studies of transition-metal halide magnetic materials. Notably, the magnetic ordering in some transition-metal compounds, such as monolayer 1T-$CrTe_2$ [52], can be highly sensitive to the choice of Hubbard U. Additional spin-polarized HSE06 calculations were performed for pristine monolayer $CuPdBr_3$ to benchmark the magnetic ground state. Interestingly, HSE06 predicts the FM state to be lower in energy than the AF-Zigzag configuration, whereas the PBE + U calculations consistently favor the AF-Zigzag state. This difference suggests that monolayer $CuPdBr_3$ is located close to the competition boundary between the FM and AF-Zigzag magnetic states, and that the predicted magnetic ground state is sensitive to the treatment of exchange-correlation effects. Nevertheless, systematic Hubbard-U dependence tests demonstrate that, within the PBE + U framework adopted throughout this work, the AF-Zigzag ground state remains robust over a broad and physically reasonable range of U values. Therefore, all subsequent investigations, including the electronic structures, magnetic exchange interactions, carrier-induced magnetic phase transition, and bipolar magnetic semiconducting behavior, are consistently carried out within this self-consistent computational framework. For the production calculations, we adopt $U_{\text{eff}}(\text{Pd}) = 2.0\,\text{eV}$ and $U_{\text{eff}}(\text{Cu}) = 0.0$ eV; finite $U_{\text{eff}}(\text{Cu})$ values were considered only in additional sensitivity tests and were not used in the production calculations. The corresponding results are provided in the Supplemental Material [46].

Here, biaxial compressive and tensile strains are applied to tune the magnetic properties. The strain is defined as $\frac{a-a_0}{a_0} \times 100\%$, where a represents the lattice constant under strain,

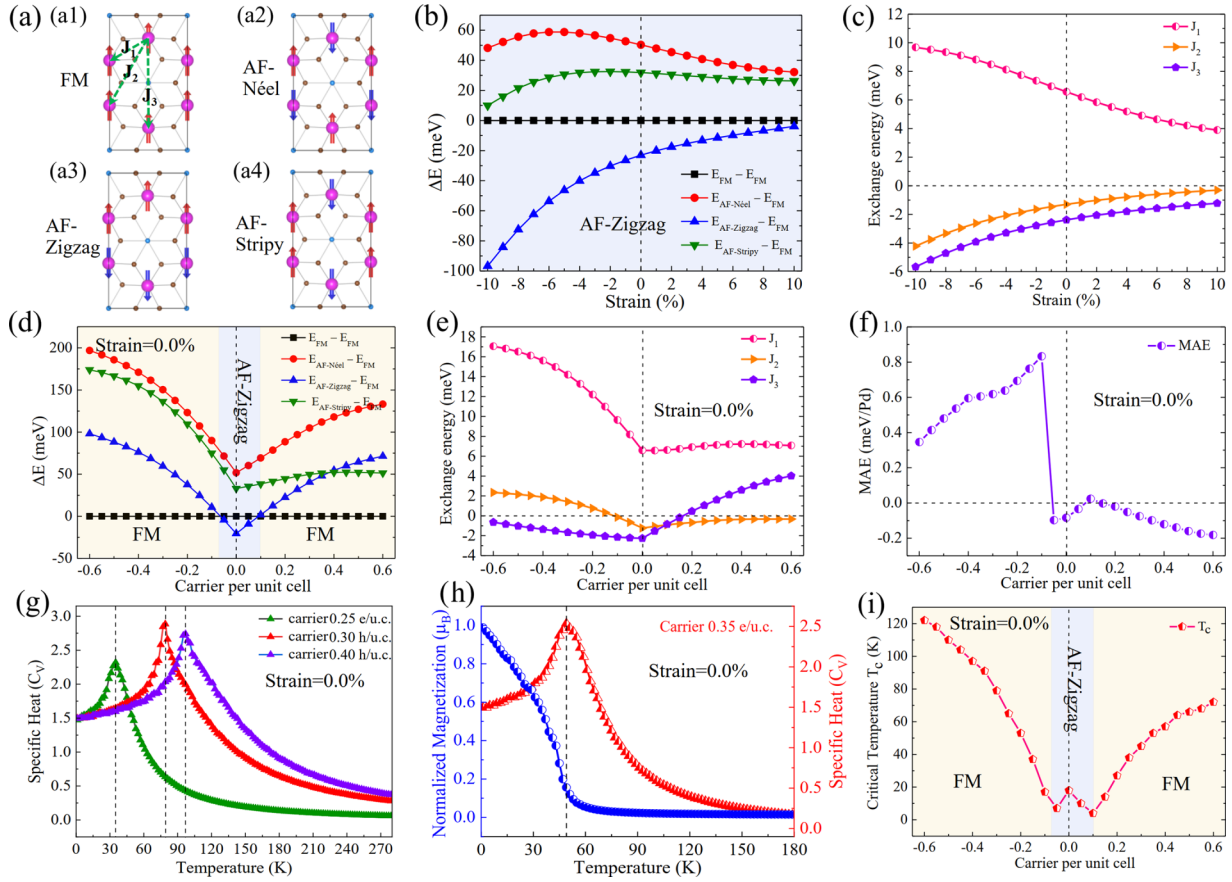


FIG. 2. (a) Four considered magnetic configurations: FM (a1), AF-Néel (a2), AF-Zigzag (a3), and AF-Stripy (a4). The red (blue) arrows in (a) denote the up (down) spins. (b) Energy difference (ΔE) between magnetic configurations of monolayer $CuPdBr_3$ as a function of strain. (c) Exchange interactions J_1, J_2, and J_3 as a function of strain. (d)–(f) Energy difference ΔE (d), exchange interaction parameters (e), and MAEs (f) as a function of carrier doping concentration for monolayer $CuPdBr_3$. (g) Specific heat capacities C_V as a function of temperature for monolayer $CuPdBr_3$, with carrier doping concentrations of 0.25 e/u.c., 0.3 h/u.c., and 0.4 h/u.c., respectively. (h) The normalized magnetic moment and specific heat capacity of monolayer $CuPdBr_3$ with 0.35 e/u.c. (i) Critical temperature (T_C) of monolayer $CuPdBr_3$ as a function of carrier doping concentration.

and a_0 denotes the equilibrium lattice constant. Figure 2(b) shows the calculated energy differences (ΔE) as a function of strain, revealing that $E_{\text{AF-Néel}}-E_{\text{FM}}$ and $E_{\text{AF-Stripy}}-E_{\text{FM}}$ remain positive, while $E_{\text{AF-Zigzag}}-E_{\text{FM}}$ stays negative. Notably, $E_{\text{AF-Zigzag}}-E_{\text{FM}}$ decreases rapidly with increasing compressive strain, indicating enhanced stability of the AF-Zigzag state. Furthermore, Fig. 2(b) illustrates that the obtained AF-Zigzag magnetic ground state in monolayer $CuPdBr_3$ remains robust against strain.

Previous studies [38–40] have shown that carrier doping is an effective strategy for tuning the magnetic properties of 2D magnetic materials. Inspired by these findings, we systematically investigate the magnetic behavior of monolayer $CuPdBr_3$ under varying carrier doping concentrations. The total energies of the four different magnetic configurations for the carrier-doped monolayer $CuPdBr_3$ are calculated by adding or removing some electrons from the calculated cell and neutralizing the system with a homogeneous charge background. The carrier density up to $\sim 10^{15}$ cm^{-2} has already been achieved in experiments [53,54]. In our calculations, the corresponding maximum doping concentration is 1.51×10^{14} cm^{-2}, which can be experimentally realized through currently advanced gating technologies. Figure 2(d) displays the calculated ΔE as a function of carrier doping concentration. The magnetic phase diagram in Fig. 2(d) shows that a magnetic phase transition from the AF-Zigzag state to the FM state can be triggered when the electron doping concentration exceeds 0.1 electrons per unit cell (0.1 e/u.c.) or the hole doping concentration exceeds 0.08 holes per unit cell (0.08 h/u.c.) in monolayer $CuPdBr_3$. To exclude possible artifacts arising from the charged-slab approach, we further examined the differential charge density distributions and spin-polarized band structures at representative carrier concentrations. The induced carriers are mainly localized within the $CuPdBr_3$ layer without forming artificial vacuum states (see Fig. S5 in the Supplemental Material [46]), confirming the intrinsic origin of the carrier-induced magnetic phase transition. To verify that the carrier-induced magnetic phase transition is not affected by spurious electrostatic interactions between periodically repeated charged slabs, we further examined the convergence of the magnetic energy differences with respect to the vacuum thickness. As shown in Fig. S7 of the Supplemental Material [46], calculations performed using vacuum thicknesses of 15, 20, 25, and 30 Å for representative carrier

concentrations (0.0 e/u.c., 0.5 e/u.c., and 0.5 h/u.c.) show nearly identical energy differences among the four magnetic configurations. These results demonstrate that the predicted AF-Zigzag to FM magnetic phase transition is well converged with respect to the vacuum thickness and is not an artifact arising from interactions between periodically repeated charged slabs.

We further investigate the strain dependence of the carrier-induced magnetic transition to examine the robustness of the proposed carrier-doping-induced magnetic switching against structural perturbations. Figures S12(a) and S13(a) in the Supplemental Material [46] present the calculated magnetic phase diagrams as a function of carrier doping concentration for monolayer $CuPdBr_3$ under 5.0% tensile strain (strain = 5.0%) and 3.0% compressive strain (strain = −3.0%), respectively. The results indicate that the carrier-doping-induced magnetic phase transition from the AF-Zigzag state to the FM state in monolayer $CuPdBr_3$ remains robust against strain.

The magnetic anisotropy energy (MAE) is an important parameter for 2D magnetic materials. The MAE per Pd atom for monolayer $CuPdBr_3$ is determined using the formula $\mathrm{MAE} = (E_{[100]} - E_{[001]})/2$, where $E_{[100]}$ and $E_{[001]}$ are the total energies of the unit cell with magnetization aligned along the [100] and [001] directions, respectively. The [100] and [001] directions correspond to magnetization parallel and perpendicular to the 2D monolayer plane, respectively. A positive MAE (MAE > 0) indicates an out-of-plane easy axis, whereas a negative MAE (MAE < 0) indicates an in-plane easy axis. For undoped monolayer $CuPdBr_3$, the MAE is −84.0 μeV/Pd, indicating that the easy axis lies in the in-plane direction, as shown in Fig. 2(f). In the FM state with a hole doping concentration of 0.3 h/u.c., the MAE increases to 618.0 μeV/Pd, suggesting that hole doping can switch the easy axis from in-plane to out-of-plane with a significant MAE enhancement, as shown in Fig. 2(f). For FM states induced by electron doping, the easy axis remains in the in-plane direction. The abrupt change in MAE observed in Fig. 2(f) is caused by the magnetic phase transition.

To describe the 2D magnetic structure of monolayer $CuPdBr_3$, we employ the Heisenberg spin Hamiltonian on a 2D honeycomb lattice, expressed as

$$H = -J_1 \sum_{\langle ij \rangle} \vec{S}_i \cdot \vec{S}_j - J_2 \sum_{\langle\langle ij \rangle\rangle} \vec{S}_i \cdot \vec{S}_j - J_3 \sum_{\langle\langle\langle ij \rangle\rangle\rangle} \vec{S}_i \cdot \vec{S}_j - D \sum_i \left(S_i^z\right)^2 - D_{\parallel} \sum_i \left(S_i^x\right)^2, \quad (1)$$

where J_1, J_2, and J_3 denote the exchange interactions between the NN, next NN (2NN), and third NN (3NN) spins, respectively. D represents the out-of-plane magnetic anisotropy, while $D_{\parallel}$ denotes a weak in-plane anisotropy that lifts the residual continuous degeneracy within the easy plane. The inclusion of $D_{\parallel}$ is particularly important for the treatment of finite-temperature magnetic order in the easy-plane regime of a 2D magnetic system. To determine the parameters J_1, J_2, and J_3, we map the DFT-calculated total energies of the four different magnetic configurations, as illustrated in Figs. 2(a1)–2(a4), onto the Heisenberg spin Hamiltonian. These configurations are modeled using a rectangular supercell ($Cu_4Pd_4Br_{12}$). The parameters are then derived from the following equations:

$$E_{\mathrm{FM/Néel}} = E_0 - (\pm 6J_1 + 12J_2 \pm 6J_3)|\vec{S}|^2, \quad (2)$$

$$E_{\mathrm{Zigzag/Stripy}} = E_0 - (\pm 2J_1 - 4J_2 \mp 6J_3)|\vec{S}|^2, \quad (3)$$

where E_{FM}, $E_{\mathrm{Néel}}$, E_{Zigzag}, and E_{Stripy} are the spin-polarized DFT total energies of the corresponding magnetic configurations calculated using the magnetic supercell ($Cu_4Pd_4Br_{12}$), and E_0 is the spin-configuration-independent energy. The parameter $D = \frac{\mathrm{MAE}}{|\vec{S}|^2}$. Here, the spin $|\vec{S}|$ is set to 1.0 ($|\vec{S}| = 1.0$). To understand the microscopic origin of the AF-Zigzag ground state of monolayer $CuPdBr_3$, we analyzed the extracted exchange parameters within the classical J_1-J_2-J_3 Heisenberg model. The obtained exchange constants ($J_1 = 6.57$ meV, $J_2 = -1.30$ meV, and $J_3 = -2.38$ meV) indicate that the NN FM interaction competes with the AFM 2NN and 3NN interactions. Such competing exchange interactions stabilize the AF-Zigzag magnetic order obtained from our total-energy calculations. Similar exchange-driven stabilization of AF-Zigzag magnetic order has been discussed within the classical honeycomb J_1-J_2-J_3 Heisenberg model [55]. It should be noted that Ref. [55] adopts a different sign convention for the exchange Hamiltonian. As shown in Fig. 2(c), J_2 and J_3 remain negative under all strain conditions, and their absolute values increase as the strain decreases from 10% to −10%. In contrast, J_1 remains positive and also increases with decreasing strain. These strain-dependent behaviors of J_1, J_2, and J_3 indicate that the AF-Zigzag magnetic ground state in monolayer $CuPdBr_3$ is robust against strain. Figure 2(e) presents the variations of J_1, J_2, and J_3 in monolayer $CuPdBr_3$ as a function of carrier doping concentration. With increasing electron or hole doping concentration, the AFM coupling gradually weakens, whereas the FM coupling strengthens, ultimately driving a magnetic phase transition from the AF-Zigzag state to the FM state.

Using the exchange interaction parameters J_1, J_2, and J_3, together with the out-of-plane and in-plane anisotropy parameters D and $D_{\parallel}$, respectively, obtained from first-principles calculations and the weak symmetry-breaking in-plane anisotropy introduced for the easy-plane magnetic regime, the T_C of monolayer $CuPdBr_3$ are estimated by classical MC simulations based on the anisotropic 2D Heisenberg model with the Metropolis algorithm. A $60 \times 60 \times 1$ 2D honeycomb lattice and 10^6 MC steps for each temperature are used. Importantly, the present spin Hamiltonian explicitly includes both the out-of-plane anisotropy D and the weak in-plane anisotropy $D_{\parallel}$ [56]. The latter lifts the residual continuous in-plane spin degeneracy in the easy-plane magnetic regime and is therefore included to satisfy the finite-temperature ordering requirement for a strictly 2D magnetic system. The out-of-plane magnetic anisotropy energy D employed in the MC simulations was obtained from fully converged first-principles calculations. As demonstrated by the convergence tests with respect to the k-point sampling, plane-wave cutoff energy, and electronic smearing parameter (Fig. S8 in the Supplemental Material [46]), the adopted computational parameters ($11 \times 11 \times 1$ k-mesh,

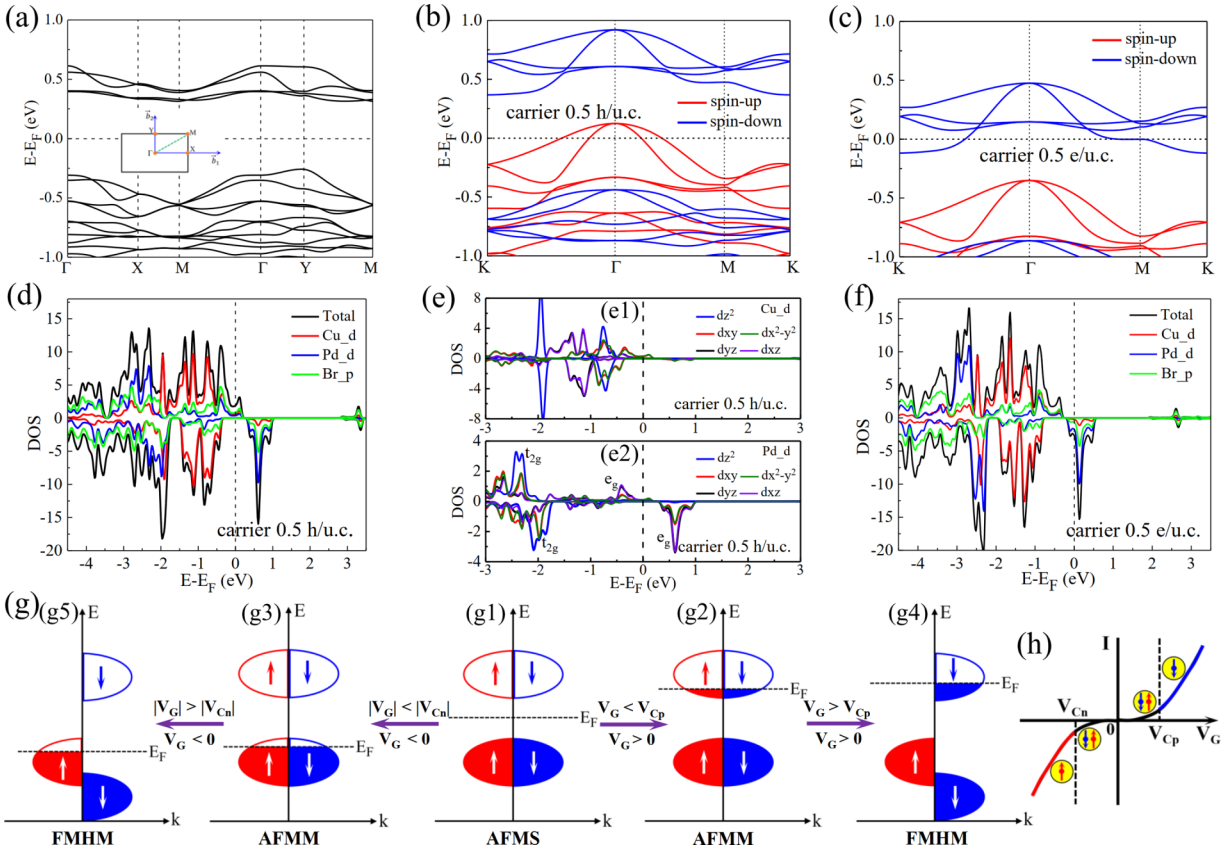


FIG. 3. (a) Band structure of monolayer $CuPdBr_3$ in the AF-Zigzag state. The inset shows the corresponding first Brillouin zone. (b), (c) Spin-polarized band structures of monolayer $CuPdBr_3$ with a carrier doping concentration of 0.5 h/u.c. (b), and 0.5 e/u.c. (c). The red and blue curves in (b) and (c) denote the spin-up and spin-down bands, respectively. (d) Densities of states (DOS) of monolayer $CuPdBr_3$ with a carrier doping concentration of 0.5 h/u.c. (e) The corresponding partial densities of states (PDOS) of (d). (e1) and (e2) are the PDOS of Cu d and Pd d orbitals, respectively. (f) DOS of monolayer $CuPdBr_3$ with a carrier doping concentration of 0.5 e/u.c. (g1) Schematic spin-resolved DOS of monolayer $CuPdBr_3$ with AFMS state. The spin-up and spin-down states are denoted in red and blue, respectively. (g2), (g3) Schematic DOS under an applied positive gate voltage (g2) in the range $0 < V_G < V_{Cp}$, and negative gate voltage (g3) in the range $V_{Cn} < V_G < 0$. V_{Cp} (V_{Cn}) denotes the critical gate voltage for AF-Zigzag state to FM state magnetic phase transition under electron (hole) doping. (g4), (g5) Schematic DOS under an applied positive gate voltage (g4) in the range $V_G > V_{Cp} > 0$, and negative gate voltage (g5) in the range $V_G < V_{Cn} < 0$. (h) Schematic plot of the spin-dependent current with respect to the applied gate voltage V_G.

ENCUT = 550 eV, and SIGMA = 0.05 eV) provide well-converged MAE values.

The calculated specific heat capacity C_V in Fig. 2(g) shows that the T_C of the monolayer $CuPdBr_3$ in FM state with a carrier doping concentration of 0.25 e/u.c., 0.3 h/u.c., and 0.4 h/u.c. is 37, 79, and 97 K, respectively. For monolayer $CuPdBr_3$ in the AF-Zigzag state without carrier doping, the estimated T_C is 18 K. Figure 2(i) displays the calculated T_C as a function of carrier doping concentration, showing that the thermal stability of the FM state increases approximately linearly with doping concentration. Moreover, the calculated T_C as a function of carrier doping concentration under strain = 5.0% and strain = −3.0% monolayer $CuPdBr_3$ are provided in Figs. S12(f) and S13(f) of the Supplemental Material [46]. These results demonstrate that the enhanced thermal stability of the carrier-induced FM state and its approximately linear dependence on carrier concentration remain robust against moderate lattice strain.

C. Electronic structures and bipolar magnetic semiconductor behavior

Figure 3(a) shows the band structure of monolayer $CuPdBr_3$ in its AF-Zigzag magnetic ground state, showing it to be a 2D AFM semiconductor with an indirect band gap of 572.1 meV. The spin-polarized band structure of monolayer $CuPdBr_3$ in the FM state is plotted in Fig. S9(a) of the Supplemental Material [46], where the VBM and CBM originate from the spin-up and spin-down channels, respectively. Furthermore, to examine the influence of the Hubbard correction on the Cu 3d states, we additionally calculated the electronic band structure using U_{eff}(Cu) = 3.0 eV while keeping U_{eff}(Pd) = 2.0 eV unchanged. As shown in Figs. S9(a) and S11(a) in the Supplemental Material [46], the band structures in the vicinity of the E_F are nearly identical to those obtained with U_{eff}(Cu) = 0.0 eV, confirming that the Hubbard correction on Cu has a negligible influence on the electronic structure relevant to the present work.

Figures 3(b) and 3(c) present the spin-polarized band structures of monolayer $CuPdBr_3$ with a carrier doping concentration of 0.5 h/u.c. and 0.5 e/u.c., respectively. The results indicate that both hole-doped and electron-doped monolayer $CuPdBr_3$ in the FM state exhibit half-metallicity, with the spin-up channel crossing the E_F under hole doping [Fig. 3(b)] and the spin-down channel crossing the E_F under electron doping [Fig. 3(c)], thereby enabling single-spin-channel transport. This carrier-doping-induced magnetic phase transition, combined with a spintronic band structure, identifies AFM monolayer $CuPdBr_3$ as a novel antiferromagnet-based BMS. To further verify the robustness of the predicted BMS behavior, representative HSE06 calculations were performed for both hole- and electron-doped cases. The HSE06 results consistently reproduce the spin-selective conducting channels characteristic of the BMS state, demonstrating that the predicted BMS behavior is robust with respect to the choice of exchange-correlation functional (see Sec. III in the Supplemental Material [46]). The band structures shown in Figs. S12(g) to S12(i) and Figs. S13(g) to S13(i) of the Supplemental Material [46] reveal that the proposed novel BMS behavior in monolayer $CuPdBr_3$ is robust against strain. Compared to conventional BMSs that exhibit spin-polarized band structures before carrier doping [11,40], the BMS behavior observed in AFM monolayer $CuPdBr_3$ is remarkably unique. In its intrinsic state, the material features a spin-degenerate AFM band structure. Upon carrier doping, a magnetic phase transition is induced, accompanied by the emergence of BMS behavior characterized by carrier-dependent single-spin-channel transport with opposite spin orientations.

As illustrated in Fig. 3(d), the spin-up states near the E_F are mainly contributed by Br p states, with additional contributions from Pd d states and Cu d states. The DOS for carrier doping concentration of 0.5 e/u.c., presented in Fig. 3(f), shows that the spin-down states near the E_F are primarily derived from Pd d states, coupled with hybridization from Br p states. Due to the presence of C_3 point symmetry in the crystal structure [Fig. 1(a)], the Pd $4d$ and Cu $3d$ orbitals are split into three groups: d_{z^2}, (d_{xy}, $d_{x^2-y^2}$), and (d_{xz}, d_{yz}), as clearly depicted in the PDOS in Figs. 3(e1) and 3(e2). Additionally, within an approximate octahedral crystal field [Fig. 1(b2)], the Pd $4d$ orbitals split into t_{2g} and e_g groups, as labeled in Fig. 3(e2). For the Pd atom, the three spin-up t_{2g}, two spin-up e_g, and three spin-down t_{2g} orbitals are occupied, while the two spin-down e_g orbitals remain unoccupied, which makes a local magnetic moment of approximately 2.0 μ_B for each Pd atom. In contrast, nearly all of the five spin-up and five spin-down $3d$ orbitals of the Cu atom are fully occupied, as illustrated in Fig. 3(e1), resulting in an almost negligible local magnetic moment for each Cu atom.

Figure 3(g1) depicts the schematic spin-resolved DOS of monolayer $CuPdBr_3$ in the AFM semiconductor (AFMS) state. Figures 3(g2) and 3(g3) plot the AFM metal (AFMM) states induced by an applied positive gate voltage V_G within $0 < V_G < V_{Cp}$ [Fig. 3(g2)] and a negative gate voltage V_G within $V_{Cn} < V_G < 0$ [Fig. 3(g3)], where the carriers remain spin-degenerate. Here, V_{Cp} (V_{Cn}) denotes the critical gate voltage for the magnetic phase transition from the AF-Zigzag state to the FM state induced by electron (hole) doping, as shown in Fig. 2(d). Figures 3(g4) and 3(g5) plot the FM half-metal (FMHF) states induced by an applied positive gate voltage V_G in the range $V_G > V_{Cp} > 0$ [Fig. 3(g4)] and a negative gate voltage V_G in the range $V_G < V_{Cn} < 0$ [Fig. 3(g5)], where the spin-down and spin-up single-spin conducting channels are realized in Figs. 3(g4) and 3(g5), respectively. Collectively, Figs. 3(g1)–3(g5) clearly illustrate the carrier-doping-driven BMS behavior in the proposed AFM monolayer semiconductor. Additionally, the schematic plot of the spin-dependent current with respect to the applied gate voltage V_G is shown in Fig. 3(h).

Based on the BMS behavior revealed in Figs. 3(g) and 3(h), we further propose a conceptual design of antiferromagnet-based spin-FET, with the corresponding schematic diagrams illustrated in Fig. 4. The source and drain electrodes considered in this conceptual device design are assumed to be FMHMs, possessing spin-up conducting channels in Figs. 4(a)–4(c) and spin-down conducting channels in Figs. 4(d)–4(f). For the monolayer $CuPdBr_3$ channel material between the source and drain electrodes, when the applied gate voltage V_G is "Low" ($V_{Cn} < V_G < V_{Cp}$), the carriers remain spin-degenerate, as illustrated in Figs. 3(g2) and 3(g3). When a positive gate voltage V_G is applied and becomes "High" ($V_G > V_{Cp} > 0$), the spin-down channel crosses the E_F, thereby enabling single-spin-channel transport, as shown in Fig. 3(g4). Conversely, under a negative "High" gate voltage ($V_G < V_{Cn} < 0$), the spin-up channel crosses the Fermi level, enabling single-spin-channel transport, as shown in Fig. 3(g5). Based on these gate-controlled spin polarization characteristics, the proposed spin-FET configurations are expected to exhibit different spin-selective transport behaviors. Specifically, when V_G is "Low" ($V_{Cn} < V_G < V_{Cp}$), the configuration shown in Fig. 4(a) corresponds to an expected "ON" transport configuration. Under positive "High" gate voltage ($V_G > V_{Cp} > 0$), the configuration in Fig. 4(b) corresponds to an expected "OFF" transport configuration due to the spin mismatch between the channel and the spin-filtering electrodes. Under negative "High" gate voltage ($V_G < V_{Cn} < 0$), the configuration in Fig. 4(c) corresponds to an expected "ON" transport configuration. Similarly, the configurations shown in Figs. 4(d), 4(e), and 4(f) are expected to exhibit "ON", "ON", and "OFF" transport behaviors, respectively. Here, the "ON"/"OFF" transport configurations are inferred from the intrinsic spin-polarized electronic structures and spin-filtering characteristics of the proposed device architecture. A quantitative evaluation of the transport performance, including interface effects and spin-dependent transmission, requires further nonequilibrium Green's function (NEGF)-based calculations, which are beyond the scope of the present work.

D. Ferromagnetic half-metal with large anomalous Hall effect

Figure 5(a) shows the spin-polarized band structure of monolayer $CuPdBr_3$ in the FM state. Two quadratic non-Dirac band degeneracies, originating from the spin-up and spin-down channels, respectively, are formed around the Γ point, as highlighted by the two yellow-shaded regions. After including SOC, these quadratic non-Dirac band degeneracies are lifted, resulting in sizable SOC-induced energy gaps around

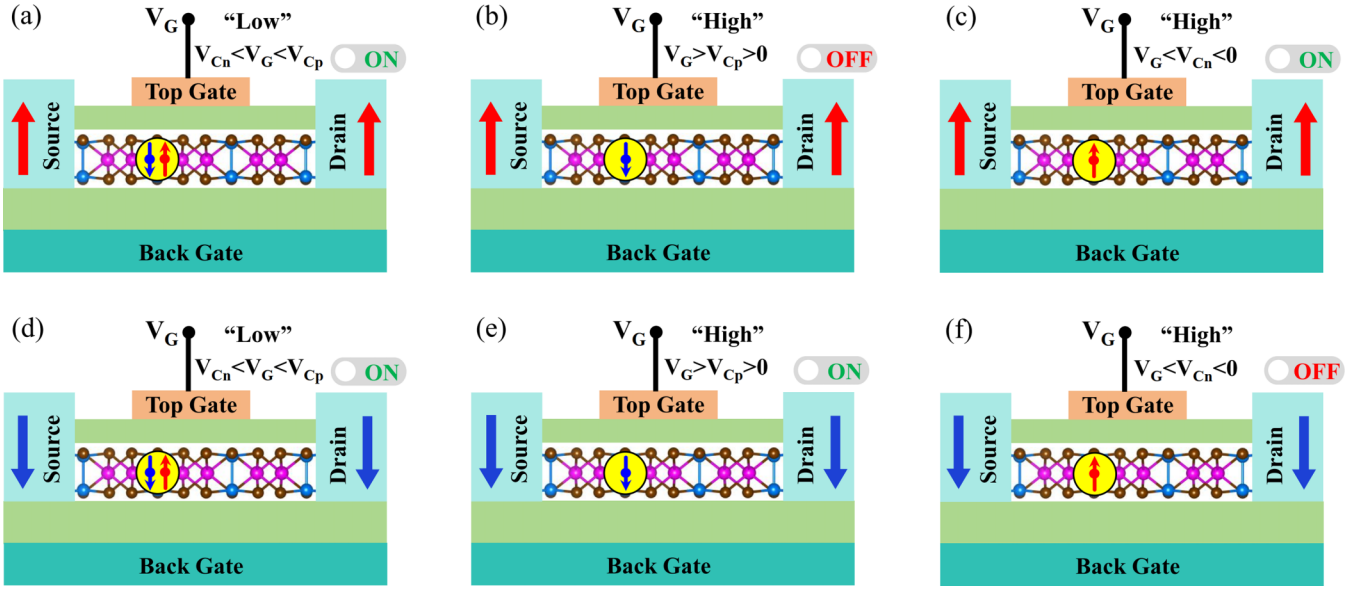


FIG. 4. Schematic illustration of the proposed spin-FET concept based on the BMS behavior of AFM monolayer $CuPdBr_3$. (a)–(c) The source and drain electrodes are assumed to be FMHMs with spin-up conducting channels. When the gate voltage is in the "Low" voltage regime ($V_{Cn} < V_G < V_{Cp}$), the channel is spin-degenerate and the conceptual device operation is illustrated in (a). Under positive "High" electron doping ($V_G > V_{Cp} > 0$), the spin-down channel becomes conducting, corresponding to the spin-mismatch state shown in (b). Under negative "High" hole doping ($V_G < V_{Cn} < 0$), the spin-up channel becomes conducting, giving rise to the spin-matching state illustrated in (c). (d)–(f) The source and drain electrodes are assumed to be FMHMs with spin-down conducting channels. The corresponding gate-controlled spin matching/mismatching configurations are schematically illustrated in (d)–(f). These diagrams illustrate a conceptual device operation mechanism based on the carrier-doping-induced single-spin-channel transport of the BMS state.

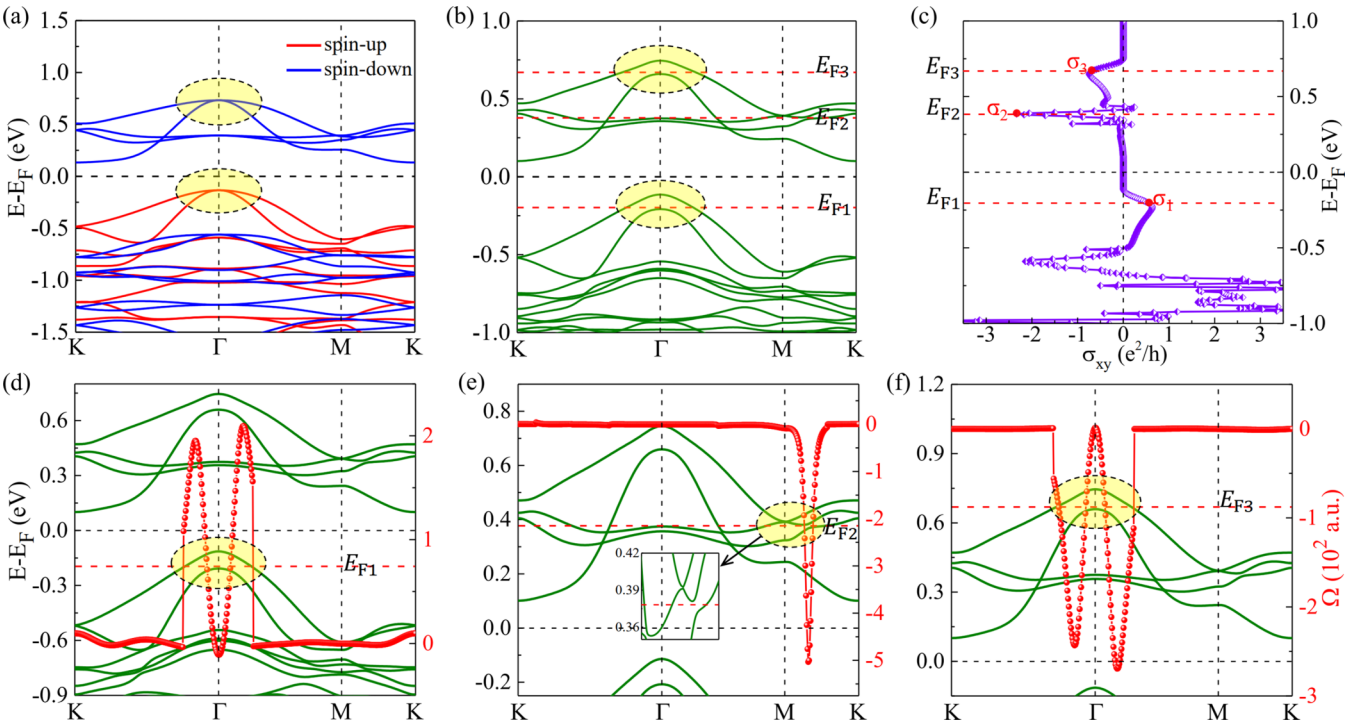


FIG. 5. (a) Spin-polarized band structure of monolayer $CuPdBr_3$ in the FM state. (b) The corresponding band structure from (a) with SOC included. (c) Anomalous Hall conductivity σ_{xy} as a function of the E_F position. The points σ_1, σ_2, and σ_3, correspond to σ_{xy} values when E_F is positioned at E_{F1}, E_{F2}, and E_{F3}, respectively. (d)–(f) The calculated Berry curvatures when E_F is set to E_{F1} (d), E_{F2} (e), and E_{F3} (f). The olive curves in (d)–(f) represent the SOC band structures.

the Γ point, as shown in Fig. 5(b). Previous theoretical studies [41,57–63] have demonstrated that SOC-induced gaps associated with quadratic non-Dirac band degeneracies possess local nontrivial band topology. Owing to the quadratic nature of the non-Dirac band degeneracy, SOC efficiently lifts the band crossing and redistributes the Berry curvature [$\Omega(\mathbf{k})$] into a narrow momentum region around the Γ point, generating pronounced $\Omega(\mathbf{k})$ hot spots. Therefore, the SOC-induced local topological gap around the spin-polarized non-Dirac band degeneracy provides the microscopic origin of the enhanced $\Omega(\mathbf{k})$ in monolayer $CuPdBr_3$.

It should be emphasized that the present system is not a QAH insulator under the equilibrium electronic structure. Although SOC opens local topological gaps around the non-Dirac band degeneracies, no global insulating gap is formed because other bands still cross the E_F. Consequently, a quantized Chern insulating state cannot be realized under the present electronic structure. Nevertheless, if the E_F is tuned into the SOC-induced local gap highlighted by the yellow-shaded regions in Fig. 5(b), the $\Omega(\mathbf{k})$ around the Γ point becomes significantly enhanced, leading to a large anomalous Hall conductivity (σ_{xy}). Therefore, the SOC-induced local topological gap associated with the spin-polarized non-Dirac bands constitutes the microscopic mechanism responsible for the predicted large anomalous Hall response. The realization of a large anomalous Hall conductivity is of considerable importance for both fundamental studies and potential spintronic applications of 2D magnetic materials. Based on the magnetic phase diagram in Fig. 2(d) and band structures in Figs. 3(b) and 3(c), tuning monolayer $CuPdBr_3$ into the FM state results in an FM half-metallic phase. In this phase, the SOC-induced band structure aligns with the bands shown in Fig. 5(b). Furthermore, the position of the E_F can be adjusted via hole doping to fall within the valence bands or via electron doping to fall within the conduction bands.

The Berry curvatures and anomalous Hall conductivity are calculated to investigate the anomalous Hall effect of the carrier doped FMHM monolayer $CuPdBr_3$. The Berry curvatures are calculated by [64,65]

$$\Omega(\mathbf{k}) = \sum_n f_n \Omega_n(\mathbf{k}), \tag{4}$$

$$\Omega_n(\mathbf{k}) = -2\mathrm{Im} \sum_{m \neq n} \frac{\hbar^2 \langle \psi_{n\mathbf{k}} | v_x | \psi_{m\mathbf{k}} \rangle \langle \psi_{m\mathbf{k}} | v_y | \psi_{n\mathbf{k}} \rangle}{(E_m - E_n)^2}, \tag{5}$$

where f_n is the Fermi-Dirac distribution function, $v_{x(y)}$ are the velocity operators, E_n is the eigenvalue of the Bloch functions $|\psi_{n\mathbf{k}}\rangle$, and the summation is over all the occupied states. The anomalous Hall conductivity σ_{xy} can be obtained by integrating the Berry curvatures over the first Brillouin zone, as $\sigma_{xy} = \frac{e^2}{2\pi\hbar} \sum_n \int_{BZ} d^2k \Omega_n$. Figure 5(c) displays the calculated σ_{xy} as a function of the E_F position. The three red dots denote the representative values σ_1, σ_2, and σ_3, corresponding to the selected E_F positions E_{F1}, E_{F2}, and E_{F3} in Fig. 5(c), respectively. These representative E_F positions are chosen to elucidate the microscopic origins of the anomalous Hall conductivity associated with different SOC-induced local band gaps in the electronic structure.

Figures 5(d) and 5(f) show the calculated $\Omega(\mathbf{k})$ distributions with the E_F placed at E_{F1} and E_{F3}, respectively, with large positive [Fig. 5(d)] and negative [Fig. 5(f)] values of $\Omega(\mathbf{k})$ distributed around the SOC-induced local energy gap around the non-Dirac Γ point. By integrating $\Omega(\mathbf{k})$ over the first BZ, large σ_{xy} of $\sigma_1 = 0.63\, e^2/h$ and $\sigma_3 = -0.74\, e^2/h$ are obtained. Notably, as illustrated in Fig. 5(c), the obtained large σ_{xy} remains positive with significant values around the E_{F1} (σ_1). It is worth noting that the E_F at E_{F1} corresponds to a hole concentration of approximately 0.20 h/u.c., which lies within the carrier-doping range investigated in the present work. Therefore, the large positive anomalous Hall conductivity around E_{F1} is expected to be experimentally accessible through electrostatic carrier doping. Moreover, the electronic band structures around the E_F, including the quadratic non-Dirac band degeneracies at the Γ point and the corresponding SOC-induced local energy gaps, remain essentially unchanged for different reasonable Hubbard parameters (Fig. S6 in the Supplemental Material [46]), indicating that the physical mechanism responsible for the enhanced Berry curvature and anomalous Hall conductivity is qualitatively robust. The obtained anomalous Hall conductivity of approximately $0.63\, e^2/h$ is comparable to those reported for several representative 2D FM materials, such as carrier-doped monolayer CrI_3 [66], monolayer CrBi [67], and Chern-insulating monolayers exhibiting $C = 1$ QAH states [20,41,68], although it is smaller than the $C = 4$ QAH state predicted for $CoBr_2$ [69].

Figure 5(e) presents the $\Omega(\mathbf{k})$ distribution with the E_F placed at the representative position E_{F2}. In this case, the dominant negative $\Omega(\mathbf{k})$ originates mainly from the SOC-induced small local energy gap along the M-K path [see the inset of Fig. 5(e)], resulting in $\sigma_2 = -2.33\, e^2/h$. The E_F positions E_{F2} and E_{F3} are introduced here as representative examples to illustrate the different microscopic mechanisms contributing to the anomalous Hall conductivity, rather than experimentally accessible carrier-doping states. Overall, these results demonstrate that SOC-induced local band gaps associated with both the quadratic non-Dirac band degeneracies around the Γ point and the avoided band crossings along the M-K path can generate pronounced $\Omega(\mathbf{k})$ and consequently large σ_{xy}. In particular, the large σ_{xy} associated with the experimentally accessible E_{F1} suggests that carrier-doped monolayer $CuPdBr_3$ is a promising platform for realizing electrically tunable anomalous Hall transport and spin-dependent Hall devices.

IV. CONCLUSIONS

In summary, we have systematically studied the electronic structures, magnetic properties, and spintronic behaviors of monolayer $CuPdBr_3$ using first-principles calculations. Our results show that monolayer $CuPdBr_3$ is an indirect band gap semiconductor with an AF-Zigzag magnetic ground state that is robust against strain. Notably, carrier doping can effectively induce a magnetic phase transition from the AF-Zigzag state to the FM state. The stability of the FM state is enhanced by increasing either the electron or hole doping concentration, and the T_C can be increased to approximately 100 K. Remarkably, carrier-doping-induced AFM monolayer $CuPdBr_3$ exhibits a novel BMS behavior, where

hole and electron doping give rise to FMHM states with spin-up and spin-down conducting channels, respectively. A conceptual spin-FET design based on the carrier-doping-induced BMS behavior of AFM monolayer $CuPdBr_3$ is proposed. Furthermore, for carrier-doped monolayer $CuPdBr_3$ in the FM state, the SOC induces band gaps at the non-Dirac band degeneracies at the Γ point, leading to large anomalous Hall conductivity. These findings establish monolayer $CuPdBr_3$ as a promising 2D material for spintronic applications, particularly in the design of spin-FETs and spin-dependent Hall-based devices. Our work offers valuable insights into tuning magnetism and electronic properties in 2D AFM materials, which may inspire future experimental studies and potential applications in antiferromagnet-based spintronics.

ACKNOWLEDGMENTS

This work was supported by National Natural Science Foundation of China (Grants No. 11904250, No. 12474155, and No. 11747137), Zhejiang Provincial Natural Science Foundation of China (Grant No. LR25A040001), and Qing Lan Project of Jiangsu Province.

DATA AVAILABILITY

The data that support the findings of this article are not publicly available upon publication because it is not technically feasible and/or the cost of preparing, depositing, and hosting the data would be prohibitive within the terms of this research project. The data are available from the authors upon reasonable request.

[1] A. K. Geim and K. S. Novoselov, The rise of graphene, Nat. Mater. **6**, 183 (2007).

[2] S. Cahangirov, M. Topsakal, E. Aktürk, H. Şahin, and S. Ciraci, Two- and one-dimensional honeycomb structures of silicon and germanium, Phys. Rev. Lett. **102**, 236804 (2009).

[3] C. R. Dean, A. F. Young, I. Meric, C. Lee, L. Wang, S. Sorgenfrei, K. Watanabe, T. Taniguchi, P. Kim, K. L. Shepard, and J. Hone, Boron nitride substrates for high-quality graphene electronics, Nat. Nanotechnol. **5**, 722 (2010).

[4] L. Li, Y. Yu, G. Ye, Q. Ge, X. Ou, H. Wu, D. L. Feng, X. H. Chen, and Y. B. Zhang, Black phosphorus field-effect transistors, Nat. Nanotechnol. **9**, 372 (2014).

[5] F. Reis, G. Li, L. Dudy, M. Bauernfeind, S. Glass, W. Hanke, R. Thomale, J. Schäfer, and R. Claessen, Bismuthene on a SiC substrate: A candidate for a high-temperature quantum spin Hall material, Science **357**, 287 (2017).

[6] K. F. Mak, C. Lee, J. Hone, J. Shan, and T. F. Heinz, Atomically thin MoS_2: A new direct-gap semiconductor, Phys. Rev. Lett. **105**, 136805 (2010).

[7] Q. H. Wang, K. Kalantar-Zadeh, A. Kis, J. N. Coleman, and M. S. Strano, Electronics and optoelectronics of two-dimensional transition metal dichalcogenides, Nat. Nanotechnol. **7**, 699 (2012).

[8] X. X. Li and J. L. Yang, First-principles design of spintronics materials, Natl. Sci. Rev. **3**, 365 (2016).

[9] Y. Guo, B. Wang, X. Zhang, S. Yuan, L. Ma, and J. L. Wang, Magnetic two-dimensional layered crystals meet with ferromagnetic semiconductors, InfoMat. **2**, 639 (2020).

[10] R. A. de Groot, F. M. Mueller, P. G. van Engen, and K. H. J. Buschow, New class of materials: Half-metallic ferromagnets, Phys. Rev. Lett. **50**, 2024 (1983).

[11] X. X. Li, X. J. Wu, Z. Y. Li, J. L. Yang, and J. G. Hou, Bipolar magnetic semiconductors: A new class of spintronics materials, Nanoscale **4**, 5680 (2012).

[12] X. X. Li and J. L. Yang, $CrXTe_3$ (X = Si, Ge) nanosheets: Two dimensional intrinsic ferromagnetic semiconductors, J. Mater. Chem. C **2**, 7071 (2014).

[13] N. Sivadas, M. W. Daniels, R. H. Swendsen, S. Okamoto, and D. Xiao, Magnetic ground state of semiconducting transition-metal trichalcogenide monolayers, Phys. Rev. B **91**, 235425 (2015).

[14] B. L. Chittari, Y. Park, D. Lee, M. Han, A. H. MacDonald, E. Hwang, and J. Jung, Electronic and magnetic properties of single-layer MPX_3 metal phosphorous trichalcogenides, Phys. Rev. B **94**, 184428 (2016).

[15] W. B. Zhang, Q. Qu, P. Zhu, and C. H. Lam, Robust intrinsic ferromagnetism and half semiconductivity in stable two-dimensional single-layer chromium trihalides, J. Mater. Chem. C **3**, 12457 (2015).

[16] Q. Sun and N. Kioussis, Prediction of manganese trihalides as two-dimensional Dirac half-metals, Phys. Rev. B **97**, 094408 (2018).

[17] X.-L. Sheng and B. K. Nikolić, Monolayer of the 5*d* transition metal trichloride $OsCl_3$: A playground for two-dimensional magnetism, room-temperature quantum anomalous Hall effect, and topological phase transitions, Phys. Rev. B **95**, 201402(R) (2017).

[18] J. He, X. Li, P. Lyu, and P. Nachtigall, Near-room-temperature Chern insulator and Dirac spin-gapless semiconductor: Nickel chloride monolayer, Nanoscale **9**, 2246 (2017).

[19] Y. P. Wang, S. Li, C. W. Zhang, S. F. Zhang, W. Ji, P. Li, and P. Wang, High-temperature Dirac half-metal $PdCl_3$: A promising candidate for realizing quantum anomalous Hall effect, J. Mater. Chem. C **6**, 10284 (2018).

[20] J. Y. You, Z. Zhang, B. Gu, and G. Su, Two-dimensional room-temperature ferromagnetic semiconductors with quantum anomalous Hall effect, Phys. Rev. Appl. **12**, 024063 (2019).

[21] M. H. Zhang, C. W. Zhang, P. J. Wang, and S. S. Li, Prediction of high-temperature Chern insulator with half-metallic edge states in asymmetry-functionalized stanene, Nanoscale **10**, 20226 (2018).

[22] Y. Liang, Y. D. Ma, P. Zhao, H. Wang, B. B. Huang, and Y. Dai, High-temperature quantum anomalous Hall insulator in two-dimensional Bi_2ON, Appl. Phys. Lett. **116**, 162402 (2020).

[23] S. C. Wu, G. C. Shan, and B. H. Yan, Prediction of near-room-temperature quantum anomalous Hall effect on honeycomb materials, Phys. Rev. Lett. **113**, 256401 (2014).

[24] T. Zhou, J. Y. Zhang, B. Zhao, H. S. Zhang, and Z. Q. Yang, Quantum spin-quantum anomalous Hall insulators and topological transitions in functionalized Sb(111) monolayers, Nano Lett. **15**, 5149 (2015).

[25] T. Zhou, J. Zhang, H. Jiang, I. Žutić, and Z. Yang, Giant spin-valley polarization and multiple Hall effect in functionalized bismuth monolayers, npj Quantum Mater. **3**, 39 (2018).

[26] G. Xu, T. Zhou, B. Scharf, and I. Žutić, Optically probing tunable band topology in atomic monolayers, Phys. Rev. Lett. **125**, 157402 (2020).

[27] J. Qi, H. Wang, X. Chen, and X. Qian, Two-dimensional multiferroic semiconductors with coexisting ferroelectricity and ferromagnetism, Appl. Phys. Lett. **113**, 043102 (2018).

[28] C. Hua, H. Bai, Y. Zheng, Z. Xu, S. A. Yang, Y. Lu, and S. Wei, Strong coupled magnetic and electric ordering in monolayer of metal thio(seleno)phosphates, Chin. Phys. Lett. **38**, 077501 (2021).

[29] X. Duan, H. Wang, X. Chen, and J. Qi, Multiple polarization phases and strong magnetoelectric coupling in the layered transition metal phosphorus chalcogenides TMP_2X_6 (T = Cu, Ag; M = Cr, V; X = S, Se) by controlling the interlayer interaction and dimension, Phys. Rev. B **106**, 115403 (2022).

[30] L. Wang, Y. P. Shi, M. F. Liu, A. Zhang, Y. L. Hong, R. H. Li, Q. Gao, M. X. Chen, W. C. Ren, H. M. Cheng, Y. Y. Li, and X. Q. Chen, Intercalated architecture of MA_2Z_4 family layered van der Waals materials with emerging topological magnetic and superconducting properties, Nat. Commun. **12**, 2361 (2021).

[31] J. Li, Y. Li, S. Du, Z. Wang, B. L. Gu, S. C. Zhang, K. He, W. Duan, and Y. Xu, Intrinsic magnetic topological insulators in van der Waals layered $MnBi_2Te_4$-family materials, Sci. Adv. **5**, eaaw5685 (2019).

[32] D. Q. Zhang, M. J. Shi, T. S. Zhu, D. Y. Xing, H. J. Zhang, and J. Wang, Topological axion states in the magnetic insulator $MnBi_2Te_4$ with the quantized magnetoelectric effect, Phys. Rev. Lett. **122**, 206401 (2019).

[33] X. Duan, J. Zhang, Z. Zhu, Y. Liu, Z. Zhang, I. Žutić, and T. Zhou, Antiferroelectric altermagnets: Antiferroelectricity alters magnets, Phys. Rev. Lett. **134**, 106801 (2025).

[34] Z. Zhu, X. Duan, J. Zhang, B. Hao, I. Žutić, and T. Zhou, Two-dimensional ferroelectric altermagnets: From model to material realization, Nano Lett. **25**, 9456 (2025).

[35] B. Huang, G. Clark, E. Navarro-Moratalla, D. R. Klein, R. Cheng, K. L. Seyler, D. Zhong, E. Schmidgall, M. A. McGuire, D. H. Cobden, W. Yao, D. Xiao, P. Jarillo-Herrero, and X. D. Xu, Layer-dependent ferromagnetism in a van der Waals crystal down to the monolayer limit, Nature (London) **546**, 270 (2017).

[36] C. Gong, L. Li, Z. Li, H. Ji, A. Stern, Y. Xia, T. Cao, W. Bao, C. Wang, Y. Wang, Z. Q. Qiu, R. J. Cava, S. G. Louie, J. Xia, and X. Zhang, Discovery of intrinsic ferromagnetism in two-dimensional van der Waals crystals, Nature (London) **546**, 265 (2017).

[37] Y. J. Deng, Y. J. Yu, M. Z. Shi, Z. X. Guo, Z. H. Xu, J. Wang, X. H. Chen, and Y. B. Zhang, Quantum anomalous Hall effect in intrinsic magnetic topological insulator $MnBi_2Te_4$, Science **367**, 895 (2020).

[38] X. X. Li, X. J. Wu, and J. L. Yang, Half-metallicity in $MnPSe_3$ exfoliated nanosheet with carrier doping, J. Am. Chem. Soc. **136**, 11065 (2014).

[39] H. B. Wang, F. Fan, S. Zhu, and H. Wu, Doping enhanced ferromagnetism and induced half-metallicity in CrI_3 monolayer, Europhys. Lett. **114**, 47001 (2016).

[40] J. Y. Zhang, B. Zhao, C. L. Ma, and Z. Q. Yang, Bipolar ferromagnetic semiconductors and doping-tuned room-temperature half-metallicity in monolayer MoX_3 (X = Cl, Br, I): An HSE06 study, Phys. Rev. B **103**, 075433 (2021).

[41] Y. J. Wang, C. C. Lou, B. Zhao, C. L. Ma, and J. Y. Zhang, Doping- and strain-tuned high Curie temperature half-metallicity and quantum anomalous Hall effect in monolayer $NiAl_2S_4$ with non-Dirac and Dirac states, Phys. Rev. B **107**, 085416 (2023).

[42] P. E. Blöchl, Projector augmented-wave method, Phys. Rev. B **50**, 17953 (1994).

[43] G. Kresse and J. Furthmüller, Efficient iterative schemes for *ab initio* total-energy calculations using a plane-wave basis set, Phys. Rev. B **54**, 11169 (1996).

[44] J. P. Perdew, K. Burke, and M. Ernzerhof, Generalized gradient approximation made simple, Phys. Rev. Lett. **77**, 3865 (1996).

[45] S. L. Dudarev, G. A. Botton, S. Y. Savrasov, C. J. Humphreys, and A. P. Sutton, Electron-energy-loss spectra and the structural stability of nickel oxide: An LSDA+U study, Phys. Rev. B **57**, 1505 (1998).

[46] See Supplemental Material at http://link.aps.org/supplemental/10.1103/f1dy-6nwp for detailed information on the robustness of the magnetic ground state with respect to the Hubbard U parameters; HSE06 calculations for the pristine monolayer and representative electron- and hole-doped cases; cleavage-energy calculations; verification of the reliability of charged-slab calculations and vacuum-thickness convergence for carrier-doped monolayer $CuPdBr_3$; numerical convergence tests for the magnetic anisotropy energy; spin-polarized band structures and density of states of monolayer $CuPdBr_3$ in the FM and AF-Zigzag states; PBE + U and SOC band structures obtained with different Hubbard U values; and strain-dependent electronic and magnetic properties of monolayer $CuPdBr_3$ under 5.0% and −3.0% strain.

[47] A. Togo, F. Oba, and I. Tanaka, First-principles calculations of the ferroelastic transition between rutile-type and $CaCl_2$-type SiO_2 at high pressures, Phys. Rev. B **78**, 134106 (2008).

[48] N. Marzari and D. Vanderbilt, Maximally localized generalized Wannier functions for composite energy bands, Phys. Rev. B **56**, 12847 (1997).

[49] I. Souza, N. Marzari, and D. Vanderbilt, Maximally localized Wannier functions for entangled energy bands, Phys. Rev. B **65**, 035109 (2001).

[50] A. A. Mostofi, J. R. Yates, Y. S. Lee, I. Souza, D. Vanderbilt, and N. Marzari, Wannier90: A tool for obtaining maximally localized Wannier functions, Comput. Phys. Commun. **178**, 685 (2008).

[51] X. J. Wang, J. R. Yates, I. Souza, and D. Vanderbilt, *Ab initio* calculation of the anomalous Hall conductivity by Wannier interpolation, Phys. Rev. B **74**, 195118 (2006).

[52] H. Y. Zhu, Y. F. Gao, Y. S. Hou, Z. G. Gui, and L. Huang, Insight into strain and electronic correlation dependent magnetism in monolayer 1T-$CrTe_2$, Phys. Rev. B **108**, 144404 (2023).

[53] H. Yuan, H. Shimotani, A. Tsukazaki, A. Ohtomo, M. Kawasaki, and Y. Iwasa, High-density carrier accumulation in ZnO field-effect transistors gated by electric double layers of ionic liquids, Adv. Funct. Mater. **19**, 1046 (2009).

[54] A. S. Dhoot, C. Israel, X. Moya, N. D. Mathur, and R. H. Friend, Large electric field effect in electrolyte-gated manganites, Phys. Rev. Lett. **102**, 136402 (2009).

[55] P. H. Y. Li, R. F. Bishop, D. J. J. Farnell, and C. E. Campbell, Phase diagram of a frustrated Heisenberg antiferromagnet on the honeycomb lattice: The J_1-J_2-J_3 model, Phys. Rev. B **86**, 144404 (2012).

[56] S. Memarzadeh, M. Rezaee Roknabadi, M. Modarresi, A. Mogulkoc, and A. N. Rudenko, Role of charge doping and strain in the stabilization of in-plane ferromagnetism in monolayer VSe_2 at room temperature, 2D Mater. **8**, 035022 (2021).

[57] Q. F. Liang, R. Yu, J. Zhou, and X. Hu, Topological states of non-Dirac electrons on a triangular lattice, Phys. Rev. B **93**, 035135 (2016).

[58] J. Y. Zhang, B. Zhao, Y. Xue, T. Zhou, and Z. Q. Yang, Coupling effect of topological states and Chern insulators in two-dimensional triangular lattices, Phys. Rev. B **97**, 125430 (2018).

[59] Y. Xue, J. Y. Zhang, B. Zhao, X. Y. Wei, and Z. Q. Yang, Non-Dirac Chern insulators with large band gaps and spin-polarized edge states, Nanoscale **10**, 8569 (2018).

[60] J. Y. Zhang, B. Zhao, T. Zhou, Y. Xue, Y. Fang, C. L. Ma, and Z. Q. Yang, Topologically trivial states induced by strong spin-orbit coupling and Chern insulators in doped $X(C_21N_3H_15)$ (X = Ta, Hf) metal-organic frameworks, Phys. Rev. B **99**, 035409 (2019).

[61] J. Shen, J. Li, J. Qian, X. Duan, C. Ma, T. Zhou, and J. Zhang, Large-gap non-Dirac quantum anomalous Hall effect in nitride TlSb monolayers on nonmagnetic substrates, Phys. Rev. B **110**, 155423 (2024).

[62] Y. Xue, B. Zhao, Y. Zhu, T. Zhou, J. Y. Zhang, N. B. Li, H. Jiang, and Z. Q. Yang, Novel Chern insulators with half-metallic edge states, NPG Asia Mater. **10**, e467 (2018).

[63] S. H. Wu, J. H. Qian, X. K. Duan, X. Z. Chen, Z. Cui, J. Y. Zhang, C. L. Ma, and T. Zhou, Electrically switchable quantum anomalous and spin Hall states in two-dimensional honeycomb lattices with non-Dirac bands, Phys. Rev. B **111**, 235414 (2025).

[64] D. J. Thouless, M. Kohmoto, M. P. Nightingale, and M. den Nijs, Quantized Hall conductance in a two-dimensional periodic potential, Phys. Rev. Lett. **49**, 405 (1982).

[65] Y. G. Yao, L. Kleinman, A. H. MacDonald, J. Sinova, T. Jungwirth, D. S. Wang, E. Wang, and Q. Niu, First principles calculation of anomalous Hall conductivity in ferromagnetic bcc Fe, Phys. Rev. Lett. **92**, 037204 (2004).

[66] M. F. Zhu, H. B. Yao, L. W. Jiang, and Y. S. Zheng, Theoretical model of spintronic device based on tunable anomalous Hall conductivity of monolayer CrI_3, Appl. Phys. Lett. **116**, 022404 (2020).

[67] A. Mogulkoc, M. Modarresi, and A. N. Rudenko, Two-dimensional chromium bismuthate: A room-temperature Ising ferromagnet with tunable magneto-optical response, Phys. Rev. Appl. **15**, 064053 (2021).

[68] P. Li, Prediction of intrinsic two dimensional ferromagnetism realized quantum anomalous Hall effect, Phys. Chem. Chem. Phys. **21**, 6712 (2019).

[69] P. Chen, J. Y. Zou, and B. G. Liu, Intrinsic ferromagnetism and quantum anomalous Hall effect in a $CoBr_2$ monolayer, Phys. Chem. Chem. Phys. **19**, 13432 (2017).